**Astronomy
&
Astrophysics**

Non-thermal radio emission from O-type stars

I. HD 168112[*]

R. Blomme[1], S. Van Loo[1], M. De Becker[2], G. Rauw[2,**],
M. C. Runacres[1], D. Y. A. Setia Gunawan[3], and J. M. Chapman[3]

[1] Royal Observatory of Belgium, Ringlaan 3, 1180 Brussel, Belgium
  e-mail: Ronny.Blomme@oma.be
[2] Institut d'Astrophysique, Université de Liège, Allée du 6 Août, Bât. B5c, 4000 Liège (Sart-Tilman), Belgium
[3] Australia Telescope National Facility, PO Box 76, Epping, NSW 2121, Australia

Abstract. We present a radio lightcurve of the O5.5 III(f$^+$) star HD 168112, based on archive data from the Very Large Array (VLA) and the Australia Telescope Compact Array (ATCA). The fluxes show considerable variability and a negative spectral index, thereby confirming that HD 168112 is a non-thermal radio emitter. The non-thermal radio emission is believed to be due to synchrotron radiation from relativistic electrons that have been Fermi accelerated in shocks. For HD 168112, it is not known whether these shocks are due to a wind-wind collision in a binary system or to the intrinsic instability of the stellar wind driving mechanism. Assuming HD 168112 to be a single star, our synchrotron model shows that the velocity jump of the shocks should be very high, or there should be a very large number of shocks in the wind. Neither of these is compatible with time-dependent hydrodynamical calculations of O star winds. If, on the other hand, we assume that HD 168112 is a binary, the high velocity jump is easily explained by ascribing it to the wind-wind collision. By further assuming the star to be an eccentric binary, we can explain the observed radio variability by the colliding-wind region moving in and out of the region where free-free absorption is important. The radio data presented here show that the binary has a period of between one and two years. By combining the radio data with X-ray data, we find that the most likely period is ~1.4 yr.

Key words. stars: individual: HD 168112 – stars: early-type – stars: mass-loss – stars: winds, outflows – radio continuum: stars – radiation mechanisms: non-thermal

1. Introduction

Radio emission from most hot stars is due to the thermal free-free emission by material in their stellar winds. A significant fraction of these stars, however, also show evidence of non-thermal emission. The radio fluxes of non-thermal sources are characterized by a zero or negative spectral index[1], significant variability and a high brightness temperature (Bieging et al. 1989). White (1985) attributed the non-thermal radiation to relativistic electrons that spiral in a magnetic field and thereby emit synchrotron radiation. These electrons are accelerated by the first-order Fermi mechanism (Bell 1978) in the shocks present in the stellar wind. In a binary, the relativistic electrons are accelerated in both shocks formed by the colliding winds (Eichler & Usov 1993). In a single star, the shocks are due to the instability of the radiative driving mechanism (e.g. Owocki et al. 1988).

For Wolf-Rayet stars, Dougherty & Williams (2000) showed that non-thermal emission is strongly correlated with binarity: 7 out of the 9 non-thermal WR emitters are identified as binaries. Not all WR binaries are non-thermal emitters: if the period is sufficiently short ($P \lesssim 1$ yr), the synchrotron emission is completely absorbed by the high free-free opacity in these stellar winds.

For O stars, the link between non-thermal emission and binarity is less clear. While colliding winds are an explanation in some cases, there remain a number of apparently single O stars that are non-thermal emitters. Relativistic electrons in these stars would then be accelerated in wind-embedded shocks. Time-dependent hydrodynamical calculations confirm that the instability in the radiative driving mechanism results in a significant number of shocks (e.g. Runacres & Owocki 2005, and references therein). Models for non-thermal emission of O-type stars, based on this mechanism, have been developed by Chen & White (1994) and Van Loo et al. (2004, 2005).

The purpose of the present paper is to study the non-thermal radio emission of the apparently single star HD 168112. We do this by collecting all available archive data. We explore both the single-star and binary scenario, to see which one best explains

---

[*] Appendix A is only available in electronic form at http://www.edpsciences.org

[**] Research Associate FNRS, Belgium.

[1] The radio spectral index α is defined by $F_\nu \propto \nu^\alpha \propto \lambda^{-\alpha}$. For thermal emission $\alpha \approx +0.6$.

Table 1. The parameters of HD 168112 from the SIMBAD catalogue, Leitherer (1988), Bieging et al. (1989) and Conti & Ebbets (1977).

RA (J2000)	$18^h18^m40\overset{s}{.}868$
Dec (J2000)	$-12°06'23\overset{''}{.}37$
$T_{\rm eff}$	46 500 K
$\log L_{\rm bol}/L_\odot$	6.06
R_*	16 $R_\odot$
M_*	70 $M_\odot$
v_∞	3250 km s^{-1}
$\dot{M}$	2.5×10^{-6} $M_\odot$ yr^{-1}
distance	2 kpc
$v_{\rm rot} \sin i$	90 km s^{-1}

the characteristics of the non-thermal emission. The main characteristics we study are the radio flux levels, spectral shape and time-scale of the variability.

HD 168112 belongs to the Ser OB 2 association (Cappa et al. 2002) and lies inside NGC 6604, located at the core of the H II region S54 (Georgelin et al. 1973). The stellar parameters and wind parameters used in this paper are listed in Table 1. De Becker et al. (2004) classified HD 168112 as O5.5 III(f$^+$). They also showed that optical spectra do not reveal radial velocity variations: thus, HD 168112 is not a binary, or it has a low inclination orbit or a long period.

Abbott et al. (1985) were the first to identify HD 168112 as a non-thermal emitter. Radio observations indicate a zero or negative spectral index as well as considerable variability. Moreover, even at minimum, its 6 cm radio flux is a factor of 10 higher than that expected from free-free radiation of the mass loss rate as determined from Hα, which is a further indicator of non-thermal emission (Bieging et al. 1989; De Becker et al. 2004).

De Becker et al. presented two radio observations separated by 6 months, showing a factor of 5–7 increase. Quasi-simultaneous XMM-Newton observations show anti-correlated behaviour: there is a decrease of ∼30% in the X-ray flux. De Becker et al. interpret such behaviour as pointing to a binary scenario, where a significant fraction of the X-ray emission is produced by the hot plasma heated by the wind-wind interaction. The present paper discusses a much larger number of radio observations. These will allow us to quantify the non-thermal properties of HD 168112 and thus to better evaluate the merits of the single-star versus binary scenario.

The remainder of this paper is structured as follows. In Sect. 2 we present the data. In Sect. 3 we explore both the single-star and binary scenario and in Sect. 4 we present our conclusions.

2. Data

Tables A.1 and A.2 list the radio observations centred on, or near to, HD 168112. These data were collected from the archives of the NRAO Very Large Array[2] (VLA) and the

Australia Telescope Compact Array[3] (ATCA). Many of these observations have not been published previously. To avoid introducing systematic shifts between different data sets, we decided to re-reduce all observations in a consistent way. Details of the reduction and the measured fluxes are given in Appendix A.

2.1. Long-term variability

The VLA and ATCA fluxes at 2, 3.6, 6 and 20 cm are plotted as a function of time in Fig. 1. Not all 20 cm upper limits were included in this figure, only those which are lower than 13 mJy. The single 13 cm detection is not plotted. The 90 cm observations are not shown as they only provide upper limits. Note that there may be slight differences in wavelength for observations we classed in the same wavelength band. The exact frequencies for each observation are listed in Table A.3.

The detections at 2, 3.6 and 6 cm in Fig. 1 clearly show the variability that is an identifying characteristic of non-thermal emission. Observations differing by more than 0.4 yr show significantly different fluxes. At certain times, HD 168112 is in a low state (around year 1992.4 and 2002.2), while at other times it is in a high state (1985.0, 1993.1 and 2001.8). The flux differs by a factor of ∼20 between these states. At 1984.2 and 2002.9, the fluxes are intermediate between the two states. Although few detections have been made at 20 cm, there are some defining a high state (1985.0, 2001.8) and some of the upper limits are sufficiently sharp to confirm the presence of a low state (2002.2).

The flux variations are not due to the fact that we are resolving the wind of the star in the highest-resolution configurations. A high-resolution observation typically has a beam of $0\overset{''}{.}5$ diameter, corresponding to ∼13 000 R_* at 2 kpc distance. This value is much higher than the expected size of a synchrotron emitting region, either in the single-star or binary scenario. We also note that the 20 cm images contain another source (GPS G018.565+01.756, at ∼11′ from HD 168112): the flux of this strong source (∼50 mJy) varies by only 20% between the HD 168112 high (1985.0) and low (2002.2) state. We therefore consider that an instrumental effect is unlikely to be the explanation for the observed variability.

Figure 1 also shows that the spectral index between 3.6 (or 2) and 6 cm is negative in most cases. This is a further indication that the emission is non-thermal. The only exception is at 2002.2, where there is a large error bar that includes the thermal value ($\alpha = +0.6$). This does not mean, however, that we are observing the underlying free-free emission of the wind. As De Becker et al. (2004) already pointed out, the expected thermal flux is only 0.03 mJy at 6 cm, which is a factor of 10 lower than the observed flux. We further note that the most extreme values of the spectral index occur when the most extreme values of the flux are reached. When the flux is high, we find a very negative spectral index ($\alpha = -1.1 \pm 0.4$ at 2001.1 and
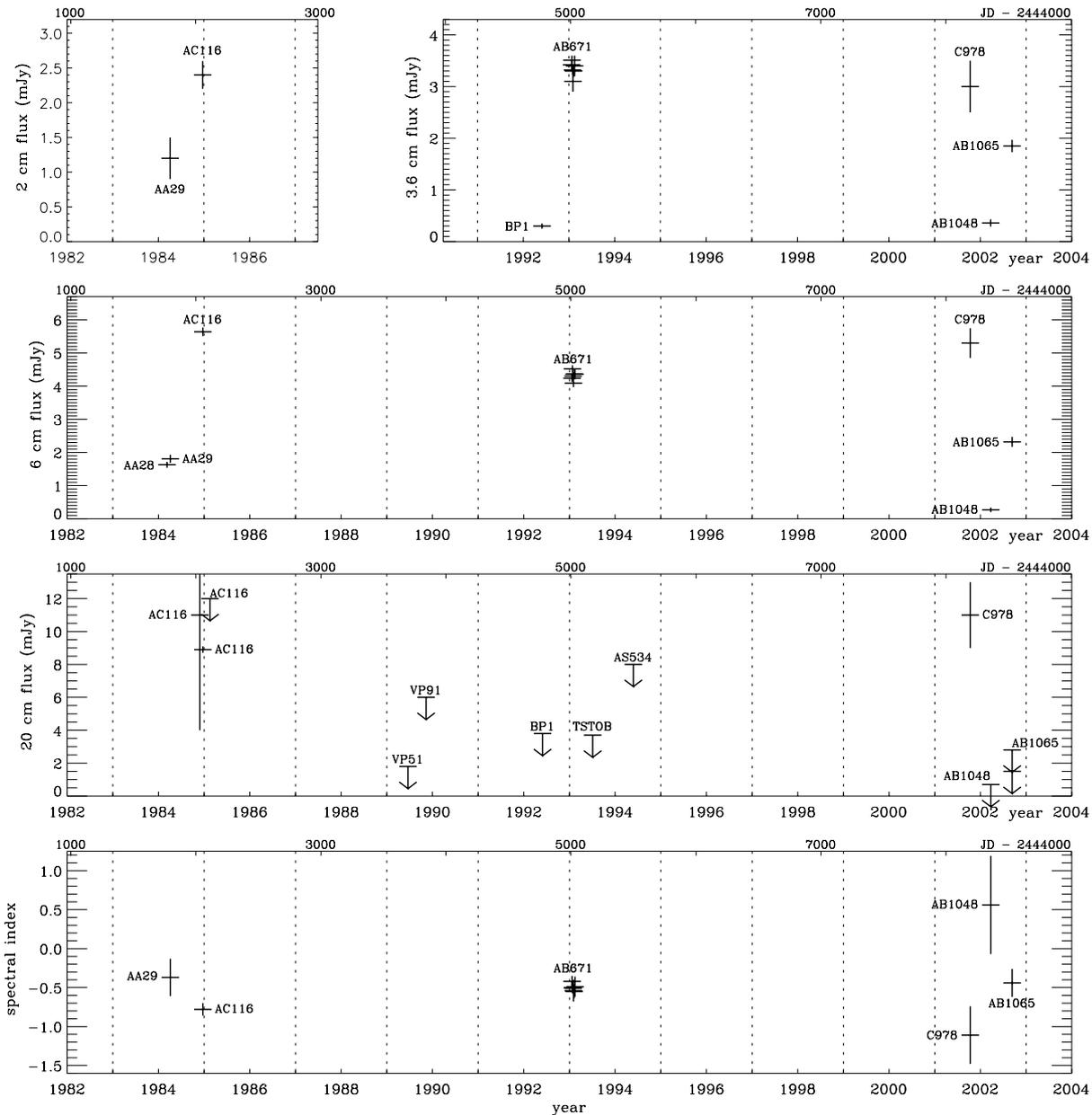
Fig. 1. The 2, 3.6, 6 and 20 cm fluxes of the VLA and ATCA archive data, plotted as a function of time. The bottom panel shows the spectral index between 3.6 and 6 cm (or 2 and 6 cm if there is no 3.6 cm observation). Observations are labelled by their programme name. Only those 20 cm upper limits below 13 mJy have been included.

$\alpha = -0.78 \pm 0.08$ at 1985.0). When the fluxes are low (2002.2), we find $\alpha = +0.6 \pm 0.6$.

The spectral index between 6 and 20 cm provides little additional information and is therefore not shown in Fig. 1. It is flatter than the 2–6 cm one at 1985.0. Around 2002.9, the 6–20 cm index is positive, indicating a turnover in the spectrum. Other observations do not allow a significant determination of the 6–20 cm spectral index.

2.2. Short-term variability

The shortest time-scales are covered by the observations with programme name AB671 (around 1993.1). These data consist of 6 observations at both 3.6 and 6 cm, spread roughly

uniformly over ~0.1 yr (1993 January 21 to February 14). Figure 2 shows that observations No. 2 and 4 deviate from the average by 5–10%. While this may suggest variability, it will be shown that this variability is spurious.

A typical test to detect an instrumental cause for apparent variability is to measure another source on the same image and see whether any flux changes are correlated to the object changes. Unfortunately, only one additional source is visible on the 3.6 and 6 cm images (at RA(J2000) = $18^h18^m40^s$, Dec(J2000) = $-12°07'$) and it is too weak (~0.5 mJy) to see if its flux changes are correlated with those of HD 168112.

A possible cause of apparent variability is the presence of large atmospheric phase changes that are not sufficiently
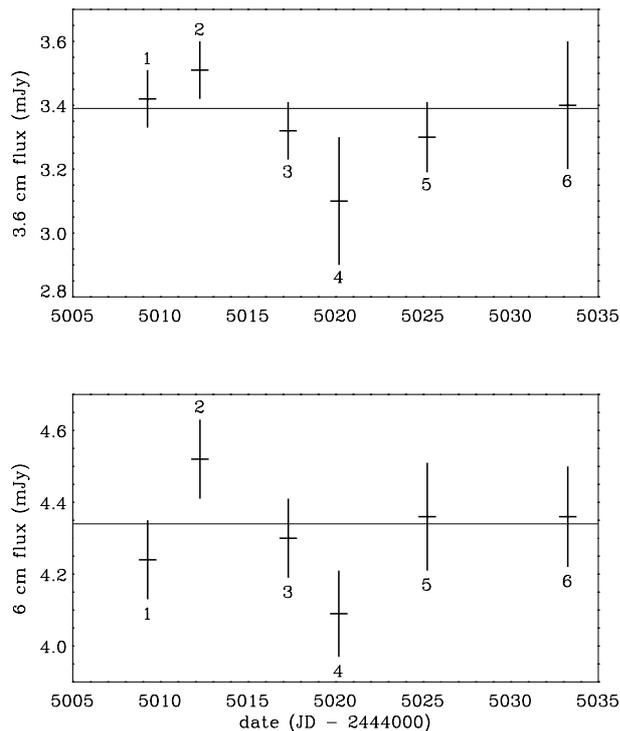
Fig. 2. The 3.6 and 6 cm fluxes of the AB671 observations. The solid line is the flux measured on the combined dataset.

well corrected for. In the reduction of the AB671 dataset, self-calibration was applied to follow the phase changes on a shorter time-scale than the phase calibrators allow (Appendix A.2). Because observation No. 4 had the lowest flux in the standard reduction (i.e. without self-calibration), we suspect that in this specific case significant phase changes occurred on shorter time-scales than could be corrected for with self-calibration. The fact that the flux for No. 4 is low is therefore not significant.

Observation No. 2 deviates from the solid line in Fig. 2 by 1.33σ at 3.6 cm and 1.64σ at 6 cm. A value of 1.64σ corresponds to a 10% (two-sided) probability of a Gaussian distribution. As we have 6 observations, it is not significant that one of them deviates by 1.64σ. We therefore conclude that we find no evidence for significant variability in the AB671 dataset. This allows us to combine all AB671 data into a single dataset and apply our reduction technique to it. The result for both wavelengths is given in Table A.1 and shown as a solid line in Fig. 2.

Some of the other data allow us to look for variability on the 0.1–0.2 yr time-scale. The two 6 cm observations AA28 and AA29 (at 1984.2) are ~0.1 yr apart and the flux is constant, within the error bars. There are three AC116 20 cm observations (around 1985), which cover a ~0.2 yr time-scale. Unfortunately, one of the observations only gives a (high) upper limit and another has a large error bar. No significant information about variability can be derived from these data.

We do find clear variability on the time-scale of 0.45 yr between the C978 (2001.8) and the AB1048 (2002.2) observation. The flux drops from the high state to the low state at 3.6, 6 and 20 cm. This provides the shortest time-scale on which the radio observations show variability.

3. Interpretation

3.1. Single-star scenario

The non-thermal radiation is due to synchrotron emission by relativistic electrons that are Fermi accelerated in shocks. In the single-star scenario, the shocks are wind-embedded (White 1985) as a consequence of the instability of the radiative driving mechanism. Time-dependent hydrodynamical calculations confirm that the wind is pervaded by shocks that can survive to large distances (e.g. Runacres & Owocki 2005, and references therein). Models for non-thermal emission of O-type stars, based on the White (1985) mechanism, have been developed by Chen & White (1994) and Van Loo et al. (2004, 2005). These models are indeed able to explain the observed non-thermal radio fluxes of Cyg OB2 No. 9 and 9 Sgr, though Van Loo et al. (2005) raise some questions about the high shock velocity jump required for their fit of the Cyg OB 2 No. 9 data.

In this section, we apply the Van Loo et al. (2005) model to HD 168112. While shocks have a large range of compression ratios and velocity jumps, Van Loo et al. showed that the strongest shocks dominate the synchrotron emission. For simplicity, the model assumes a single shock to be present in the wind. (This assumption is of minor importance as the results can be re-interpreted in terms of multiple shocks – see below.) The model is then described by only four parameters: the position of the shock R_S, the compression ratio χ and the velocity jump Δu of the shock and the surface magnetic field B_*.

In the model, the momentum distribution of the relativistic electrons is calculated taking into account the electron acceleration by the Fermi mechanism (Bell 1978) and the deceleration due to inverse-Compton and adiabatic cooling. The synchrotron-emitting relativistic electrons form a narrow layer downstream of the shock. The synchrotron flux is then calculated (including the Razin effect) and corrected for free-free absorption in the wind, giving the predicted radio flux. We assume that for this star, $v_{rot} = 250$ km s^{-1} (similar to White 1985, for Cyg OB 2 No. 9) and that the wind temperature is 0.3 times the effective temperature (Drew 1989). For further details of the model, see Van Loo et al. (2005).

By calculating a grid of models, we can see which combinations of parameters explain the observations. To constrain the fit parameters sufficiently well, it is necessary to have (nearly) simultaneous radio observations at three or more wavelengths. We applied the model to the AC116 (1984 December 21) observation, which has detections at three wavelengths (2, 6 and 20 cm). Note that this observation is representative of the high flux state of HD 168112. We calculated the fluxes at the three wavelengths for a grid of R_S, χ, Δu and B_*. The star and wind parameters needed in the model are given in Table 1. All combinations of the model parameters that fit the observations within the error bars are shown in Fig. 3.

Figure 3a shows that only moderately strong to strong shocks ($\chi = 2.7$–4), located between 220 R_* and 500 R_* can explain the observations. The surface magnetic field is less well constrained: we find results for B_* from 30 G upward, to values which are above the generally accepted detection limit for O stars (of order 100 G, Mathys 1999).
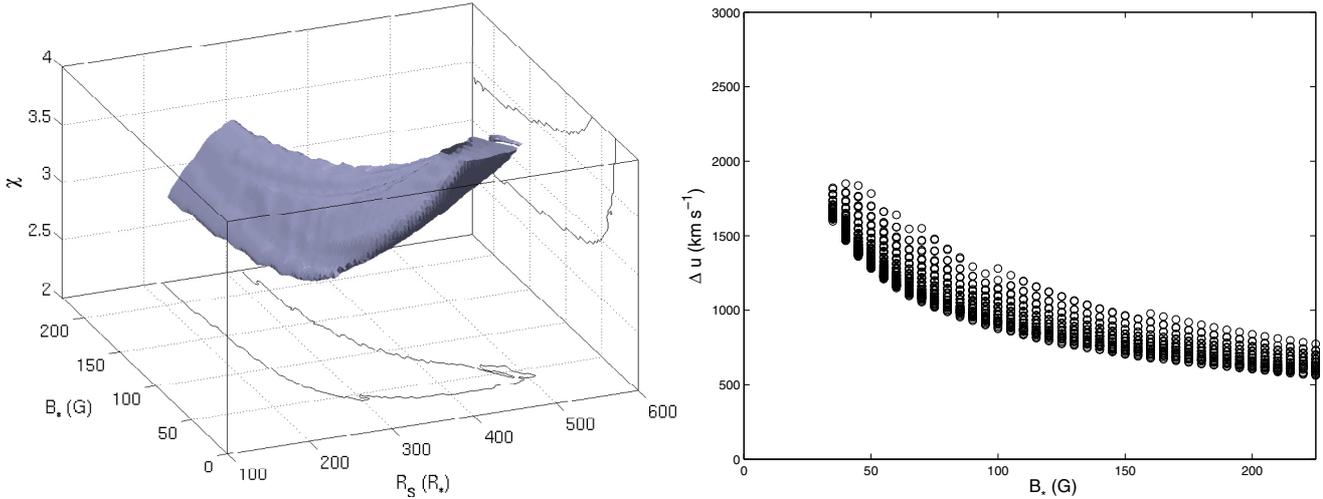
Fig. 3. a) *Left panel*: the combinations of χ, R_S and B_* that fit the AC116 (1984 December 21) observation for HD 168112 lie in the grey volume on the figure. Projections on two planes are plotted to situate the solutions in the parameter space. **b)** *Right panel*: the values for the surface magnetic field B_* and the shock velocity jump Δu are shown for all possible combinations of the model parameters that explain the radio observations of HD 168112.

The most important result, however, is that the shock velocity jump is $600-1800$ km s^{-1} (Fig. 3b). Such values are considerably higher than those found from time-dependent hydrodynamical calculations: at $200-500$ R_*, Δu is typically only 50 km s^{-1} (Runacres & Owocki 2005).

One can lower the required Δu by re-interpreting the results of this single shock model in terms of multiple shocks. Van Loo et al. (2005) showed that multiple shocks also fit the observations provided that the sum of their Δu^3 equals the single shock Δu^3 (all other parameters being the same). To attain the reasonable value of $\Delta u = 50$ km s^{-1} would require more than 1700 shocks. We cannot put these shocks at arbitrary positions in the wind (Van Loo 2005). In the single-shock model, the resulting 20 cm flux is determined by both the intrinsic synchrotron radiation and the free-free absorption. If we put the shocks in a region well beyond the location we found for the single shock, the free-free absorption will be less effective and the 20 cm flux will become higher than observed. We therefore have to put the 1700 shocks in a region near the location we found for the single shock. From hydrodynamical calculations, it is obvious that we cannot put that many shocks in so small a region.

Another observation suitable for the Van Loo et al. (2005) model is the C978 one, which provides simultaneous observations at 3.6, 6, 13 and 20 cm. The observed fluxes of 3.0, 5.3, 8.2 and 11 mJy nearly exactly follow a power law. (By fitting such a law through the four data points, we find a spectral index of -0.7 ± 0.1.) A consequence of this is that there is no significant upper bound on the shock position R_S. (Only when the larger-wavelength fluxes fall below the power-law extrapolation of the short-wavelength fluxes can a constraint on R_S be derived – see Van Loo 2005.) The fits show that a large range of shock positions and compression ratios fit the observations. As for the AC116 data, we find that the velocity jump is too high ($\Delta u \geq 500$ km s^{-1}) to be compatible with hydrodynamical models.

We also fitted the observations of the AB1065 dataset, which has detections at 3.6 and 6 cm, and a significant upper limit at 20 cm. Results from the fits show that the position of the shock is between 50 and 200 R_*. The compression ratio is not as well constrained (a consequence of having only an upper limit at 20 cm): we find $\chi \geq 2$. Solutions are found for all magnetic field strengths $B_* \geq 10$ G. Most important, however, is that the Δu values are about the same as for the AC116 dataset.

The observation AB1048 is representative of the low state. However, no significant constraints can derived from this observation. The single shock velocity jump should be at least 190 km s^{-1}. This value is lower than for the others because the general flux level for this observation is low.

The location of the AB1065 shock is more inward than the AC116 shock. This suggests a direct explanation for the difference in flux level between the two observations. The AB1065 shock is closer to the star, so the intrinsic synchrotron flux has to pass through more free-free absorbing material, resulting in a lower radio flux. If this is the correct explanation for the variability in the observed fluxes, we should expect the variability to happen on the hydrodynamical time-scale, which is of the order of 4 days (the time needed for a shock to travel 100 R_*). However, the AB671 dataset (Sect. 2.2) does not show any variability. To explain why the flux remains constant for nearly one month, we would have to invoke the fortuitous circumstance of a train of shocks, all of about equal strength, occurring during one month. Ascribing the variability in the whole dataset to differences in shock positions therefore does not appear convincing.

As an alternative cause of variability, we could consider variations in the magnetic field. Very little is known about magnetic fields in O stars, so it is difficult to make predictions on what time-scale the variability would occur. One possibility is the rotational time-scale (which is about 1–2 weeks for these stars), but this is again contradicted by the AB671 observations (Sect. 2.2).

In summary, the single-star scenario can explain the spectral shape, but has considerable difficulties explaining the flux levels, as a high velocity jump or a very large number of shocks would be required. We cannot attribute the variability to changes in the shock structure. In the single-star scenario, we therefore have to surmise that the variability is caused by an inherent variability in the magnetic field. The period of the variability is discussed in Sect. 3.2.

3.2. Binary scenario

In this section we explore the constraints the data provide assuming that HD 168112 is a colliding-wind binary. The best studied example of such a colliding-wind binary is WR 140 (White & Becker 1995) and we will use it as a guide in interpreting the present observations. The 2 cm light curve of WR 140 shows, during one period, a rising branch followed by a descending branch. At larger wavelengths, the same feature is seen, but the peak formed by the two branches becomes sharper. The light curve shows good repeatability from one period to another.

The intrinsic synchrotron radiation will depend on the separation of the two components. In an eccentric binary more synchrotron emission will be generated at periastron than at apastron. However, free-free absorption will remove some, or all, of the flux, depending on the position in the wind (i.e. on the optical depth along the ray to the observer). The *observed* radio lightcurve will therefore have a maximum at a phase different from periastron. Exactly when the maximum occurs depends on the geometry of the orbit.

For close binaries, the colliding-wind region will be completely inside the free-free radius, and we therefore expect to see no variation on the time-scale of the orbital period. This is indeed the case for Cyg OB 2 No. 5 (Miralles et al. 1994). For HD 168112, however, we may assume that it is not a close binary, otherwise De Becker et al. (2004) would have found radial velocity variations in their optical spectra, even for an unfavourable orbital inclination (see also below).

In the binary hypothesis, we therefore attribute the large radio flux changes in Fig. 1 to the orbital motion. The peaks in flux occur at 1985.0, 1993.1 and 2001.8, which are ~8.5 yr apart. The true period is much shorter than this, as is shown by the rising and descending branches of the lightcurve. In 1984–5 and 1992–3 we have a rising branch (seen in 2, 3.6 and 6 cm) lasting ~1 yr. A descending branch (seen in 3.6, 6 and 20 cm) is seen around 2002 and lasts ~0.45 yr. We therefore expect the true period to be between 1 and 2 years.

To better determine the period we tried various periods in the range 1–2 yr and plotted the 3.6 and 6 cm fluxes as a function of phase. (The 2 and 20 cm fluxes do not provide additional information as they are strongly correlated with the 3.6 and 6 cm fluxes.) We do not have a mathematical description for the expected behaviour of the fluxes as a function of time, so the quality of the phase locking was judged by eye. We checked that the lightcurve shows only one rising and one descending branch over the whole period and that fluxes at nearby phases have similar values. Trying a large number of periods we find
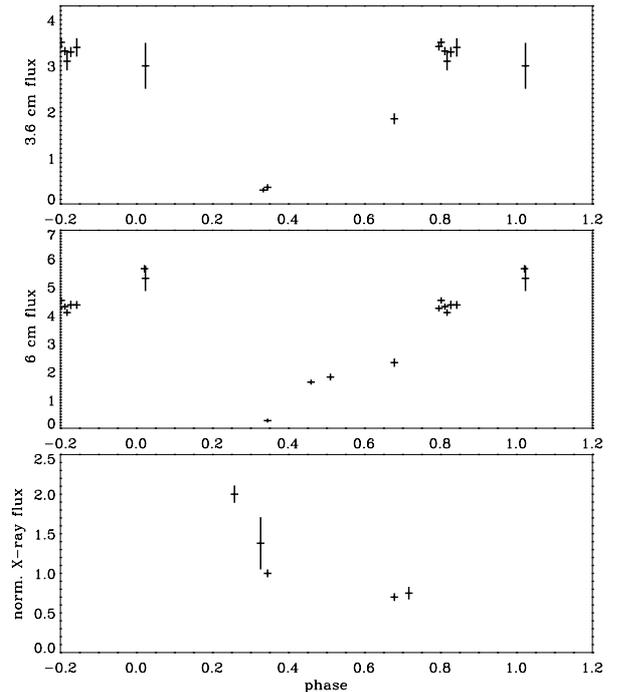

Fig. 4. The 3.6 and 6 cm radio fluxes, folded with a 1.4 yr period. The normalised X-ray fluxes from De Becker et al. (2004) are also plotted (*bottom panel*). Phase 0.0 was arbitrarily set at JD = 2 444 000.0.

that $P = 1.07$, 1.12, 1.22, 1.4 and 1.66 yr give good phase locking. The result for $P = 1.4$ yr is shown in Fig. 4.

Even the longest period proposed would result in an orbit of the companion that would remain within the free-free radius, at least if we assume the orbit to be circular. The orbit with a 1.66 yr period would have a semi-major axis of ~90 R_* (based on the mass listed in Table 1 for the primary and an assumed mass of 30 $M_\odot$ for the secondary). At a radius of 90 R_*, the radial optical depth for free-free absorption at 20 cm is ~2.5 (which can be derived from Wright & Barlow (1975), using the data from Table 1). This would absorb a large part of the intrinsic radio flux. Shorter periods would of course suffer even more free-free absorption. We therefore need to assume an eccentric orbit, so that the colliding-wind region becomes visible near apastron. Note that De Becker et al. (2004) showed that the X-ray variability of HD 168112 can be explained by a binary provided the eccentricity is ≥0.5. An eccentric binary with a 1–2 yr period is also compatible with the AB671 fluxes being constant over a one month time-scale.

X-ray data can provide some further constraints on the period. Similar to the radio, more X-ray flux is generated at periastron than at apastron. For such a wide binary seen under low inclination, the absorption in X-rays is, however, less than that at radio wavelengths. As the separation between the two components becomes smaller, the observed X-ray flux therefore increases, while the radio flux decreases (due to the increasing free-free absorption). For an eccentric binary, the passage through periastron will be fast, so we expect a sharp peak in the X-ray emission around that time.

For HD 168112, De Becker et al. (2004) present two XMM-Newton observations taken quasi-simultaneously with

VLA radio data (programmes AB1048 and AB1065). They also reanalysed three older X-ray observations. If we fold all the X-ray fluxes with the radio periods found above, we find that only the 1.4 yr period shows a reasonable behaviour for the X-ray fluxes. Figure 4 shows the X-ray data folded with the 1.4 yr period. The steeply descending fluxes around phase 0.2–0.4 could be due to the fast change in separation as the secondary moves away from periastron in the eccentric orbit. This would suggest that periastron occurs at phase ~0.2.

Clumping of the stellar wind material will not allow a shorter period, or a less eccentric orbit. This is because clumping has no effect on the optical depth, provided that we require the same (thermal) flux to be emitted. This can be seen from Abbott et al. (1981). Assuming that the density ratio of the low-density versus high-density material is zero, their Eq. (10) shows that the flux is proportional to $(\dot{M}^2/f)^{2/3}$, where f is the volume filling factor of the high-density material. The optical depth (their Eq. (9)) is proportional to $\dot{M}^2/f$. If we compare a smooth wind with a clumped wind and require both to have the same flux, they need to have the same $\dot{M}^2/f$ value, which also means that the optical depth is the same (for details, see Van Loo 2005). Clumping can also lead to the material becoming porous to radiation (Owocki et al. 2004). If we would include the effect of porosity as well, the 20 cm optical depth at 90 R_* would be smaller, allowing a shorter period, or a less eccentric orbit for the binary.

One can speculate on the nature of the companion. If it is a normal star of the same luminosity class as the O5.5 III(f$^+$) primary, the spectral type would have to be later than O5.5. It would probably not be as late as O9 since otherwise we should see low excitation lines in the spectrum that would be untypical of the primary. If the difference in magnitude becomes larger than 2.5, then the companion could be of any type (a B-star, a pre-main-sequence star of a few solar masses, ...). A compact companion would produce much brighter X-ray emission than what is observed and the spectrum would follow a blackbody rather than an optically thin spectrum. Bieging et al. (1989) already dismissed the compact companion hypothesis as improbable on evolutionary grounds.

Is the presence of a companion compatible with the fact that such a companion was not detected in the available optical spectroscopy? We checked this by exploring the parameter space of possible periods P, mass ratios $q = M_2/M_1$, eccentricities e and inclination angles i, to see which combinations give velocity changes that would remain undetected. We consider a grid of $q = 0.1, 0.4, 0.7, 1.0$, $e = 0.0, 0.5$ and $i = 15°$, $30°, 60°, 90°$. We also took into account the time-scales that are covered by the available optical data. Adopting an upper limit of 10 km s^{-1} (2 sigma) on the semi-amplitude (K) of the velocity variations, we find that for $q \geq 0.4$, the inclination should be $i < 15°$ for a period $P < 2$ yr. For $q = 0.1$, higher inclination angles are possible and even $i = 90°$ cannot be excluded. Of course, there is always the possibility that the optical spectra might have been taken at the wrong phase, so that we sample only a small part of the total velocity variation.

Thus, the observations are in agreement with HD 168112 being a (low inclination) binary, with a period of less than 2 yr. It seems that the most likely period is ~1.4 yr. The binary
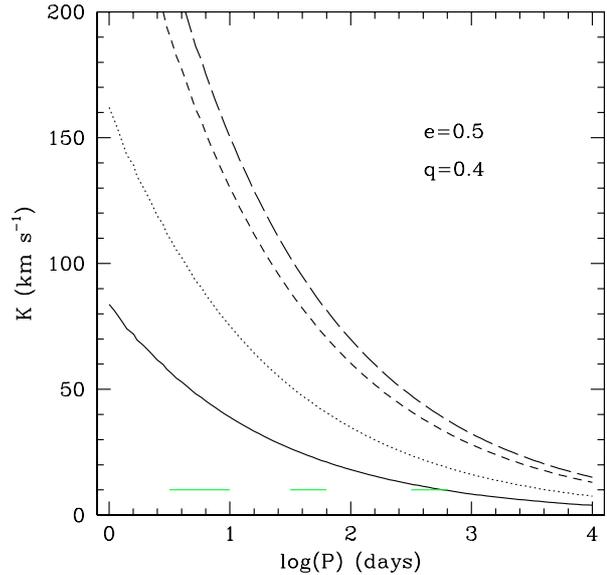

Fig. 5. The semi-amplitude K of the velocity variations as a function of period P, for eccentricity $e = 0.5$, mass ratio $q = 0.4$ and inclination $i = 15°$ (solid line), 30° (dotted), 60° (short-dashed) and 90° (long-dashed). The three horizontal lines at the 10 km s^{-1} level show the time ranges that have been covered by the available optical spectroscopy data (De Becker et al. 2004).

scenario explains the observed variability very well, as shown in Fig. 4. While we did not model the spectral shape or flux levels, we can derive some information from the single-star synchrotron model (Sect. 3.1). Even though that model is not appropriate for a binary, the location and the velocity jump of the single shock in that model are in qualitative agreement with what can be expected for a colliding-wind region (e.g. WR 147, Dougherty et al. 2003).

4. Conclusions

In this paper we studied the available VLA and ATCA radio data on HD 168112. The archive data confirm the non-thermal nature and high variability of the radio emission. Variability is present at a time-scale of 0.45 yr or more, and the fluxes can differ by a factor of ~20. No variability was found on time-scales less than 0.1 yr.

We interpreted the observations in terms of both a single-star and binary scenario. Assuming HD 168112 to be single, we applied the Van Loo et al. (2005) model to the observations. The fact that the strong shocks (which dominate the synchrotron emission) are at different positions for different times of observation was suggested as an explanation for the variability. It fails, however, to explain why the flux remained constant for about one month. An even more important problem with the single-star scenario is that the shocks need to have velocity jumps very much higher than those predicted by hydrodynamical models. As an alternative, when we forced the shocks to have an acceptable velocity jump, we found that too many shocks are required to explain the flux levels. The failure of the single-star scenario to give results compatible with hydrodynamical simulations is a major conclusion of this work.

The binary hypothesis is very successful in explaining all the observational material. The non-thermal emission is due to the colliding winds. The variability can be explained by the colliding-wind region in an eccentric binary moving in and out of the region where the free-free absorption is important. The high value found for the shock velocity jump is to be expected for a colliding-wind region. Also, the X-ray data are in agreement with this scenario. The non-detection by optical spectroscopy suggests an orbital inclination $i < 15°$. While the amount of radio data available is not large, they clearly show that the period should be between one and two years. In combination with the X-ray observations, the present data suggest that the binary period is most likely ~1.4 yr. The constraint on the period is another major conclusion of this work, and it will allow a much better planning of future observing campaigns. While the current evidence favours the binary scenario, confirmation of this and the determination of the period still need to be sought from future observations.

References

Abbott, D. C., Bieging, J. H., & Churchwell, E. 1981, ApJ, 250, 645
Abbott, D. C., Bieging, J. H., & Churchwell, E. 1985, in Radio Stars, ed. R. M. Hjellming, & D. M. Gibson (Dordrecht: D. Reidel), 219
Bell, A. R. 1978, MNRAS, 182, 147
Bieging, J. H., Abbott, D. C., & Churchwell, E. B. 1989, ApJ, 340, 518
Bridle, A. H., & Schwab, F. R. 1999, in Synthesis Imaging in Radio Astronomy II, ed. G. B. Taylor, C. L. Carilli & R. A. Perley, ASP Conf. Ser., 180, 371
Briggs, D. S. 1995, High Fidelity Deconvolution of Moderately Resolved Sources, Ph.D. Thesis, The New Mexico Institute of Mining and Technology, Socorro, New Mexico
http://www.aoc.nrao.edu/dissertations/dbriggs
Cappa, C. E., Goss, W. M., & Pineault, S. 2002, AJ, 123, 3348
Chen, W., & White, R. L. 1994, Ap&SS, 221, 259
Conti, P. S., & Ebbets, D. 1977, ApJ, 213, 438
Cornwell, T., & Fomalont, E. B. 1999, in Synthesis Imaging in Radio Astronomy II, ed. G. B. Taylor, C. L. Carilli, & R. A. Perley, ASP Conf. Ser., 180, 187
Cotton, W. D. 1999, in Synthesis Imaging in Radio Astronomy II, ed. G. B. Taylor, C. L. Carilli, & R. A. Perley, ASP Conf. Ser., 180, 357
De Becker, M., Rauw, G., Blomme, R., et al. 2004, A&A, 420, 1061
Dougherty, S. M., & Williams, P. M. 2000, MNRAS, 319, 1005
Dougherty, S. M., Pittard, J. M., Kasian, L., et al. 2003, A&A, 409, 217
Drew, J. E. 1989, ApJS, 71, 267
Eichler, D., & Usov, V. 1993, ApJ, 402, 271
Georgelin, Y. M., Georgelin, Y. P., & Roux, S. 1973, A&A, 25, 337
Leitherer, C. 1988, ApJ, 326, 356
Mathys, G. 1999, in Variable and Non-spherical Stellar Winds in Luminous Hot Stars, ed. B. Wolf, O. Stahl, & A. W. Fullerton, Lect. Notes Phys., Proc. IAU Coll., 169, 523, 95
Miralles, M. P., Rodríguez, L. F., Tapia, M., et al. 1994, A&A, 282, 547
Owocki, S. P., Castor, J. I., & Rybicki, G. B. 1988, ApJ, 335, 914
Owocki, S. P., Gayley, K. G., & Shaviv, N. J. 2004, ApJ, 616, 525
Perley, R. A., & Taylor, G. B. 2003, The VLA Calibrator Manual
http://www.aoc.nrao.edu/~gtaylor/calib.html
Phillips, R. B., & Titus, M. A. 1990, ApJ, 359, L15
Reynolds, J. 1994, A Revised Flux Scale for the AT Compact Array, ATNF Internal Report, AT/39.3/040
http://www.atnf.csiro.au/observers/memos/
d96783~1.pdf
Runacres, M. C., & Owocki, S. P. 2005, A&A, 429, 323
Sault, B., & Killeen, N. 1999, Miriad Users Guide
http://www.atnf.csiro.au/computing/software/miriad
Ulvestad, J. 2002, Eighth Synthesis Imaging Summer School, 18–25 June 2002, Socorro, New Mexico, USA
http://www.aoc.nrao.edu/events/synthesis/2002
Van Loo, S. 2005, Ph.D. Thesis, in preparation
Van Loo, S., Runacres, M. C., & Blomme, R. 2004, A&A, 418, 717
Van Loo, S., Runacres, M. C., & Blomme, R. 2005, A&A, 433, 313
White, R. L. 1985, ApJ, 289, 698
White, R. L., & Becker, R. H. 1995, ApJ, 451, 352
Wright, A. E., & Barlow, M. J. 1975, MNRAS, 170, 41

Online Material

Appendix A: Data reduction

A.1. VLA data

The data reduction was done using the Astronomical Image Processing System (AIPS), developed by the NRAO. Technical details of the reduction are listed in Table A.1 for the 2, 3.6 and 6 cm observations and Table A.2 for the 20 and 90 cm observations. Except where otherwise indicated, all observations were made in 2 sidebands (denoted IF1 and IF2), each of which has a bandwidth of 50 MHz. For the flux calibration, we followed the procedure outlined by Perley & Taylor (2003). The fluxes assigned to the flux calibrators are given in Table A.3. We then determined the instrumental gains from the phase calibrator observations, interpolated them and applied them to the observation of the source. Where needed, bad data points were flagged.

The calibrated visibilities were assigned weights using robust uniform weighting (Briggs 1995) and were then inverted by a Fourier transform to produce an image. For all reductions, the image covers most or all of the full primary beam. The image was then deconvolved using the CLEAN algorithm to remove the effect of the beam (point spread function). We stopped cleaning when the algorithm started finding about the same number of negative as positive components. On the observations made with low spatial resolution (VLA configurations C and D), some Galactic background structure can be seen. We excluded the minimum amount of observational data taken on the shortest baselines to ensure the removal of this background. In Fig. A.1 we show some typical examples of the resulting maps.

We measured the fluxes on the cleaned image using the AIPS task JMFIT to fit elliptical Gaussians to the source. The elliptical Gaussian was forced to have the major axis, minor axis and position angle equal to the beam values. For the 20 cm AC116 (1984-11-27) observation, HD 168112 is not close to the centre of the map. In that case, the flux measurement becomes more complicated. First, the sensitivity of the image decreases as one moves away from the centre ("primary beam attenuation"). The images can easily be corrected for this effect (using the task PBCOR). A second effect is beamwidth smearing (Bridle & Schwab 1999): an off-centre source is smeared out in the direction that is radial toward the centre of the image. Fortunately, this effect conserves the total flux. For this observation, we measured the flux by using an elliptical Gaussian with all parameters left free. As a check, we used the interactive task TVSTAT to integrate the flux over the area occupied by the beamwidth-smeared source. We found that both measurements were in acceptable agreement.

Usually, the measured fluxes are assigned an error bar corresponding to the root-mean-square (rms) noise in the map. The rms error bar only covers the random sources of error. To estimate some of the *systematic* errors, we redid the reduction a number of times. We excluded one antenna from the data, excluded one run (if there were at least three runs), tried natural or uniform weighting instead of robust uniform weighting or varied the extent of the taper. The error bar we assign to the measured fluxes covers the range in fluxes we thus found. In many cases this is larger than the rms error bar. We also measured the flux by determining the maximum intensity of the point source, instead of fitting an elliptical Gaussian. In most cases, both measurements agree within the error bars. The worst non-agreement is the 6 cm AC116 observation, where the maximum intensity is -2.5σ below the integrated value. Lesser effects are shown by AB1065 – 3.6 cm ($+1.2\sigma$), AA28 – 6 cm (-1.4σ) and AB671 1993-01-24 – 6 cm (-1.5σ).

The final error bar was determined by adding (in a rms sense) a 2% calibration error for the 3.6, 6, 20 and 90 cm observations and a 5% error for the 2 cm. These represent the uncertainty in the absolute calibration (Perley & Taylor 2003).

For those observations where HD 168112 was not detected, we assigned an upper limit of 3 times the rms noise measured in the map (in a small box around the source). To take into account some of the systematic effects, we also performed the various reductions described above and used the highest rms thus found to define the upper limit. When HD 168112 is offset from the centre, the rms must be measured on the image corrected for primary beam attenuation. To correct for the beamwidth smearing, we had to multiply the rms by the number of beams that a detectable beamwidth-smeared source at this position would cover. From Bridle & Schwab (1999) we find that the number of beams can be approximated by $\sqrt{1 + \beta^2}$, where:

$$\beta = \frac{\text{bandwidth (MHz)}}{\text{observing frequency (MHz)}} \times \frac{\text{offset (arcsec)}}{\text{beamwidth (arcsec)}}. \quad \text{(A.1)}$$

In some cases HD 168112 is within the primary beam on two images centred on different targets. In that case we only list the one closest to HD 168112 because this gives the smallest error bar. We did check that the flux of the other image is compatible with the flux listed. The following observations were not listed because they are of such low quality that they do not even provide a significant upper limit: BAUD (1980-07-12; 20 cm), FIX (1982-05-22; 20 cm), AC161 (1986-05-11; 90 cm), AH250 (1986-12-27 and 1987-03-19; 90 cm), AK162 (1987-03-20; 90 cm), AH299 (1988-03-24, 1988-05-02 and 1988-09-23; 90 cm), AT143 (1993-06-11; 20 cm), AL341 (1994-09-13; 90 cm) and AG626 (2002-08-14, 2002-11-23, 2002-12-07, 2003-02-23 and 2003-02-24; 90 cm).

A complication arose in the reduction of the TSTOB data. Comparing the fluxes of other sources in the field around HD 168112 across the various programmes showed that the TSTOB values are too low by a factor of ~2. Fortunately, the TSTOB programme was immediately followed by another programme (AW362) that observed the same flux calibrator at the same wavelength. Using the flux calibrator from that programme in the reduction, the TSTOB fluxes become high enough to be compatible with the others. The results in Fig. 1 and Table A.2 are based on this improved reduction.

A comparison with the literature (Bieging et al. 1989; Phillips & Titus 1990; De Becker et al. 2004) shows acceptable agreement in most cases. There is a tendency for our error bars (or upper limit in the case of Phillips & Titus) to be larger: this is due to our inclusion of systematic effects. Note also that the AB1048 and AB1065 fluxes are somewhat different from those published in De Becker et al. (2004). This is because, in the present paper, we followed the recommendation by Perley & Taylor (2003) to assign a small, but non-zero,

Table A.1. Reduction of the data at 2, 3.6 and 6 cm. Programme C978 is an ATCA observation, all others are VLA observations. Column (1) gives the programme name; (2) the date of the observation; (3) the phase calibrator (J2000 coordinates); (4) the distance of HD 168112 to the phase calibrator (degrees); (5) the integration time (in minutes) on the source; (6) the number of antennas that gave a usable signal; (7) the configuration the VLA or ATCA was in at the time of the observation; (8) the major and minor axis (both in arcsec) of the beam; (9) the position angle (degrees) of the beam; (10) the rms in the centre of the image and; (11) the measured flux (in mJy).

(1) Progr.	(2) Date	(3) Phase calibrator Name	(4) Dist.	(5) Intgr. time	(6) No. ants.	(7) Config.	(8) Beamsize (arcsec^2)	(9) PA (deg)	(10) rms (mJy)	(11) Flux (mJy)
2 cm										
AA29	1984-04-04	1733-130	11.2	22	24	C	2.3 ×1.4	13.9	0.20	1.2 ± 0.3
AC116	1984-12-21	1733-130	11.2	45	27	A	0.16×0.12	2.2	0.13	2.4 ± 0.2
3.6 cm										
BP1	1992-05-30	1733-130	11.2	43	24	C	9.2 ×4.8	−88.8	0.05	0.30 ± 0.05
AB671	1993-01-21	1811-209	9.0	19	22	A	0.33×0.21	25.8	0.05	3.42 ± 0.09
AB671	1993-01-24	1811-209	9.0	19	27	A	0.41×0.23	38.2	0.05	3.51 ± 0.09
AB671	1993-01-29	1811-209	9.0	19	26	BnA	0.91×0.50	51.9	0.05	3.32 ± 0.09
AB671	1993-02-01	1811-209	9.0	6	27	BnA	0.82×0.40	84.4	0.09	3.1 ± 0.2
AB671	1993-02-06	1811-209	9.0	19	27	BnA	0.83×0.42	68.3	0.04	3.30 ± 0.11
AB671	1993-02-14	1811-209	9.0	9	27	BnA	0.95×0.49	56.3	0.09	3.4 ± 0.2
AB671	combined						0.60×0.29	64.6	0.02	3.39 ± 0.07
C978	2001-10-11	1832-105	3.7	161	6	EW352	4.51×0.65	−1.3	0.25	3.0 ± 0.5
AB1048	2002-03-24	1832-105	3.7	11	26	A	0.31×0.25	11.3	0.06	0.36 ± 0.07
AB1065	2002-09-11	1832-105	3.7	9	26	CnB	3.0 ×2.1	47.4	0.11	1.85 ± 0.12
6 cm										
AA28	1984-03-09	1733-130	11.2	28	26	CnB	3.7 ×2.1	−87.8	0.07	1.63 ± 0.09
AA29	1984-04-04	1733-130	11.2	14	27	C	5.9 ×3.7	10.6	0.11	1.81 ± 0.12
AC116	1984-12-21	1733-130	11.2	50	27	A	0.55×0.36	−20.1	0.06	5.64 ± 0.13
AB671	1993-01-21	1811-209	9.0	19	24	A	0.73×0.68	−27.2	0.07	4.24 ± 0.11
AB671	1993-01-24	1811-209	9.0	19	27	A	0.55×0.44	9.6	0.06	4.52 ± 0.11
AB671	1993-01-29	1811-209	9.0	19	26	BnA	1.7 ×1.1	34.7	0.06	4.30 ± 0.11
AB671	1993-02-01	1811-209	9.0	6	27	BnA	1.5 ×0.81	82.5	0.09	4.09 ± 0.12
AB671	1993-02-06	1811-209	9.0	18	27	BnA	1.5 ×1.0	64.1	0.06	4.36 ± 0.15
AB671	1993-02-14	1811-209	9.0	10	27	BnA	1.7 ×0.92	51.3	0.08	4.36 ± 0.14
AB671	combined						0.91×0.47	59.1	0.03	4.34 ± 0.10
C978	2001-10-11	1832-105	3.7	161	6	EW352	7.41×1.09	−1.4	0.19	5.3 ± 0.45
AB1048	2002-03-24	1832-105	3.7	11	26	A	0.53×0.36	12.3	0.07	0.27 ± 0.07
AB1065	2002-09-11	1832-105	3.7	8	26	CnB	4.8 ×2.0	57.4	0.13	2.32 ± 0.15

weight (WTUV = 0.1) to the flux calibrator visibilities outside the usable range. There are two exceptions to the acceptable agreement. For the 2 cm AC116 (1984-12-21) observation, we have 2.4 ± 0.2 mJy, while Bieging et al. find 1.3 ± 0.1 mJy. They note an apparent increase of flux at the largest baselines. Our reduction of the data does not show such a problem, giving a higher confidence in our result. For the 6 cm AA28 (1984-03-09) observation we found 1.63 ± 0.09 mJy, while Bieging et al. list 1.3 ± 0.1 mJy. We could not find an explanation for this discrepancy.

A.2. Self-calibration

The AB671 dataset has a number of problems. The phase calibrator used has a low 3.6 cm flux, making it unsuitable for phase calibration. The time between two phase calibrations exceeds 30 min in 5 of the 6 observations, which is too long to follow the phase changes due to the atmosphere, especially in these high-resolution observations. When we applied our standard reduction, we found considerable variability in the fluxes. However, these flux variations are highly correlated with the

flux variations of HD 167971, which was observed as part of the same observing programme. At least a large part of the variability must therefore be due to atmospheric effects that were not correctly removed in the standard reduction.

We therefore decided to apply phase self-calibration (see, e.g. Cornwell & Fomalont 1999) to this set of observations. This technique is suitable for the "simple" field here, consisting of two point sources on an empty background. It allows us to follow the atmospheric phase changes on a shorter timescale than the time between two phase calibrator observations. From the known sensitivity of the VLA and the estimated flux of HD 168112, we find that a 3 min time-scale is appropriate, provided that we combine both sidebands and all Stokes polarizations and decrease the requested signal-to-noise ratio of the gain solutions to 2 (Ulvestad 2002). Ideally, we would prefer a 10 s time-scale (which is the duration of a single integration), so we could follow the phase changes even better. Unfortunately, insufficient signal would then be available for the calibration. We applied 5 iterations of phase-only calibration. No amplitude self-calibration was done because amplitude errors are relatively unimportant on the dynamic ranges of

Table A.2. Reduction of the data at 13, 20 and 90 cm. Programmes C599 and C978 are ATCA observations, all others are VLA observations. Columns are as in Table A.1; note that Col. (10) gives the rms noise for the standard reduction in the centre of the image, while upper limits in Col. (11) are based on the highest rms found in the search for systematic effects (see Appendix A.1) and are corrected for the primary beam effect and bandwidth smearing, if not in the centre of the image. Column (12) refers to the notes and, for the VLA observations, lists the width of the sidebands if different from 2×50 MHz.

(1) Progr.	(2) Date	(3) Phase calibrator Name	(4) Dist.	(5) Intgr. Time	(6) No. Ants.	(7) Config.	(8) Beamsize $(arcsec^2)$	(9) PA (deg)	(10) rms (mJy)	(11) Flux (mJy)	(12) Notes
13 cm											
C978	2001-10-11	1832-105	3.7	120	6	EW352	15. × 1.9	−1.3	0.26	8.2 ± 0.6	X
20 cm											
BOWE	1982-01-31	1743-038	11.9	13	8	A	4.2 × 1.2	75.2	7.1	<100.	B, 1 × 1.5625
BAUD	1982-02-28	1743-038	11.9	33	13	A	1.4 × 1.0	5.5	11	<55.	B, 1 × 1.5625
AC116	1984-11-27	1733-130	11.2	28	25	A	1.7 × 1.2	9.4	3.6	11 ± 7	B
AC116	1984-12-21	1733-130	11.2	10	27	A	1.7 × 1.2	3.4	0.14	8.9 ± 0.2	
AG163	1984-12-24	1743-038	11.9	1	27	A	1.8 × 1.2	−9.8	0.47	<90.	B, 2 × 25
AC116	1985-02-16	1733-130	11.2	15	25	A	1.6 × 1.2	−2.4	0.12	<12.	B
AB531	1989-05-01	1834-126	3.9	2	26	B	6.3 × 4.1	17.9	1.0	<26.	B, 1 × 50
VP51	1989-06-19	1733-130	11.2	29	25	C	15. × 10.	−14.4	0.31	<1.8	X
AG290	1989-07-20	1833-210	9.6	0	27	C	22. × 11.	−21.1	1.4	<60.	B
VP91	1989-11-10	1733-130	11.2	18	27	D	43. × 27.	−12.2	1.7	<6.	X
BP1	1992-05-30	1911-201	14.9	40	25	C	20. × 15.	−70.5	0.80	<3.8	
TSTOB	1993-07-05	1822-096	2.6	14	27	C	67. × 12.	50.2	0.84	<3.7	
AS534	1994-05-26	1822-096	2.6	5	24	BnA	4.1 × 2.3	−79.5	1.2	<8.	B, X, 1 × 3.125
AS534	1994-06-01	1822-096	2.6	4	25	BnA	4.9 × 2.1	56.8	1.6	<90.	B, X, 1 × 3.125
AC308	1996-06-09	1833-210	9.6	1	27	DnC	38. × 21.	81.1	2.4	<19.	B
AC308	1996-06-16	1833-210	9.6	1	27	DnC	40. × 20.	71.7	1.6	<18.	B
C599	1997-02-25	1934-638	54.0	89	6	6A	32. × 4.4	3.2	0.52	<23.	B
AC308	1997-10-16	1833-210	9.6	1	27	DnC	38. × 20.	84.0	2.2	<16.	B
C978	2001-10-11	1832-105	3.7	120	6	EW352	27. × 3.4	1.2	0.42	11 ± 2	X
AB1048	2002-03-24	1834-126	3.9	5	26	A	2.0 × 1.3	19.0	0.17	<0.7	
AB1065	2002-09-11	1834-126	3.9	5	26	CnB	7.1 × 3.3	40.0	0.68	<2.8	I, λ = 18 cm
AB1065	2002-09-11	1834-126	3.9	5	21	CnB	8.1 × 3.8	38.9	0.37	<1.5	λ = 20 cm
90 cm											
AH299	1988-06-21	1829+487	60.9	47	21	DnC	125. × 72.	−81.0	57	<340.	B, 2 × 3.125
AH299	1989-05-28	1829+487	60.9	57	25	CnB	50. × 37.	−65.7	13	<90.	B, 2 × 3.125

Notes:
B   Observation is not centered on HD 168112. The flux (or upper limit) has been corrected for that.
    No correction for beamwidth smearing needs to be applied to C599 (see Sect. A.3).
X   The phase calibrator is of low quality (Perley & Taylor 2003) for VP51, VP91, AS534 and C978.
I   Interference is high in the AB1065 18 cm image.

the images we have. The results presented in Figs. 1 and 2 and Table A.1 are those based on the self-calibration reduction.

To make sure that the self-calibration technique does not introduce systematic effects, we also applied it to those cases where it is not really needed. These tests show that self-calibration and the standard reduction give the same results within a few percent, provided that the self-calibration is carefully applied (i.e. not on a complicated background, no interference present in the image and a time-scale appropriate for the flux). A side effect of self-calibration is that the absolute positional information is lost.

A.3. ATCA data

The ATCA data were reduced in Miriad following the user guide (Sault & Killeen 1999). We did not reduce the 13 cm data of the C599 programme because HD 168112 is well outside the primary beam. The data were read into Miriad and corrected for self-interference of the array and for the phase difference between the X and Y channels. After reading in, the data consist of 13 frequency channels, each of 8 MHz width. The reduction then proceeds in a way similar to the VLA reduction (Appendix A.1). The use of multiple frequency channels requires us to do a bandpass calibration on the phase calibrator.

Fluxes assigned to the flux calibrator are listed in Table A.3. The programme C978 uses the phase calibrator 1832−105 (J2000), which is not recommended at 20 cm (according to the VLA Calibrator Manual, Perley & Taylor 2003). For the 13 and 20 cm observations, we therefore made a map around this calibrator. To remove structure in the background, we had to flag the shortest baselines. In our data, the phase calibrator turns out to be a point source (with a flux of 1.04 Jy at 13 cm and 0.94 Jy at 20 cm). There are no other sources in the field that have a
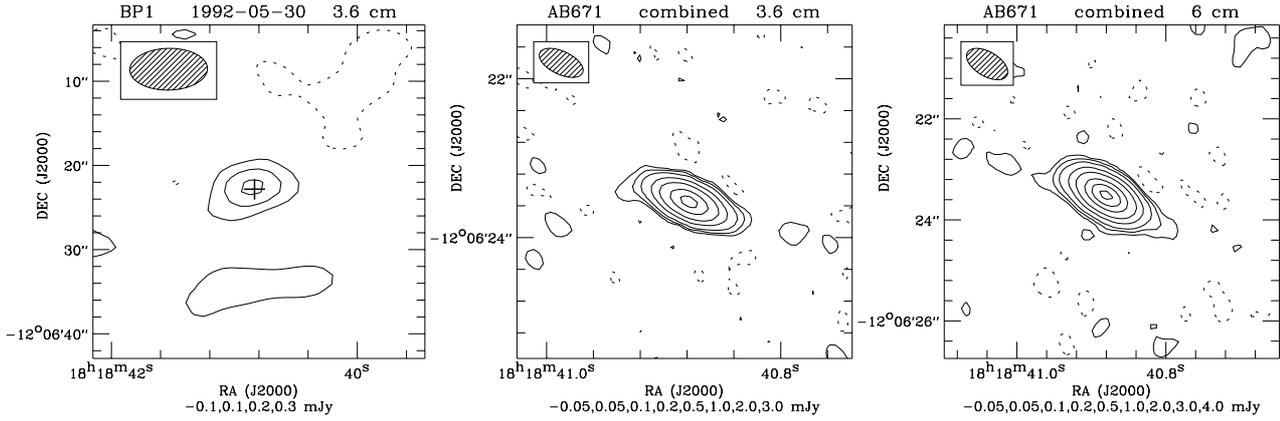
Fig. A.1. Some examples of maps of VLA archive data at 3.6 and 6 cm. The values of the contour levels are listed at the bottom of each panel. The negative contour is given by the dashed line. The first positive contour is at about twice the rms noise in the map. The beam is shown in the upper left corner. The cross indicates the optical ICRS 2000.0 position (from SIMBAD). Because self-calibration loses absolute positional information, this is not shown in the middle and right panels. Note the different spatial scales and different contour levels of the maps.
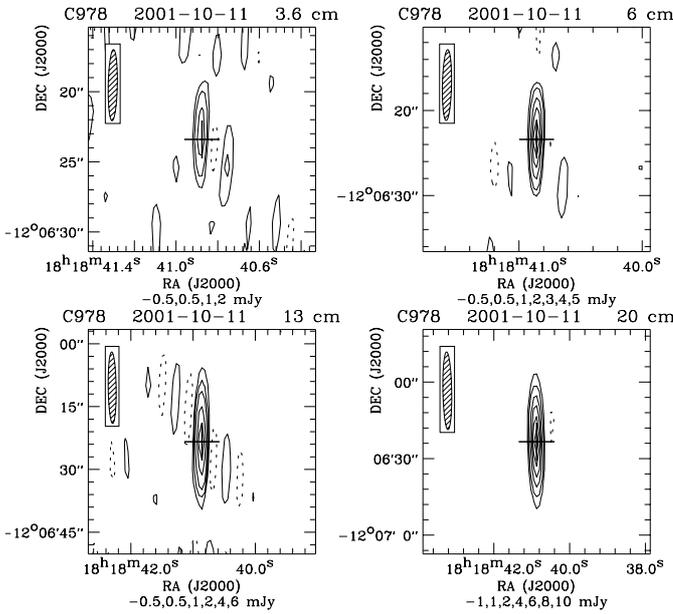

Fig. A.2. Maps of ATCA archive data where HD 168112 was detected. The values of the contour levels are listed at the bottom of each panel. The negative contour is given by the dashed line. The first positive contour is at about twice the rms noise in the map. The beam is shown in the upper left corner. The cross indicates the optical ICRS 2000.0 position (from SIMBAD). Note the different spatial scales and different contour levels of the maps.

the image, and more boxes were therefore used. We stopped cleaning when the algorithm started finding about the same number of negative as positive components. Applying this criterion, we arrive close to the theoretical rms, which is the noise calculated taking only the system temperature of the front-end receiver into account, not the calibration errors, side-lobes or any other instrumental effects. Only for the 20 cm observation do we end up with an rms level of about twice the theoretical rms. We attribute this to the more complicated background at this wavelength. Results are listed in Tables A.1 and A.2. These results include the flux calibration uncertainty of 2% and the estimated effect of systematic errors (derived in a similar way as for the VLA data). The detections are plotted in Fig. A.2.

flux higher than 0.01 Jy. Thus, we consider 1832−105 to be an acceptable calibrator for our data.

For the target observation, we also had to exclude data from the shortest baselines, to remove background structure in the resulting image. In the inversion and cleaning step, we applied multi-frequency synthesis (MFS), which compensates for the spectral index of the source across the bandwidth. An interesting consequence of MFS is that we do not have to correct for bandwidth smearing for those targets that are offset from the centre (Cotton 1999). The cleaning was applied in a box around the target. At larger wavelengths more sources are visible on

Table A.3. Fluxes of the flux calibrators used in the reduction of the archive data. Programmes C599 and C978 are ATCA observations, all others are VLA observations. The VLA flux scale is based on the 1995.2 coefficients (Perley & Taylor 2003). The ATCA flux scale is given by Reynolds (1994).

Calib.	Freq. (GHz)	Flux (Jy)	Programmes
2 cm			
3C 286	14.915	3.460	AA29, AC116
	14.965	3.452	AA29, AC116
3.6 cm			
3C 286	8.415	5.224	AB671, BP1
	8.465	5.203	AB671
3C 48	8.435	3.164	AB1048, AB1065
	8.485	3.145	AB1048, AB1065
1934-638	8.640	2.841	C978
6 cm			
3C 286	4.835	7.510	AA28, AA29, AC116, AB671
	4.885	7.462	AA28, AA29, AC116, AB671
3C 48	4.835	5.459	AB1048, AB1065
	4.885	5.405	AB1048, AB1065
1934-638	4.800	5.828	C978
13 cm			
1934-638	2.496	11.14	C978
20 cm			
3C 286	1.365	15.01	AC308
	1.435	14.65	AC308
	1.452	14.57	AG163
	1.465	14.51	AC116, AG290, AB531
	1.502	14.34	AG163
	1.515	14.28	AC116, AG290
	1.612	13.85	BAUD, BOWE, AS534
	1.665	13.63	VP91, BP1
3C 48	1.385	16.20	AB1048, AB1065, TSTOB
	1.465	15.49	AB1048, AB1065
	1.635	14.19	AB1065
	1.665	13.98	AB1065
1733-130	1.665	5.200	VP51[a]
1934-638	1.384	14.94	C599, C978
90 cm			
3C 286	0.328	25.90	AH299
	0.333	25.77	AH299

[a] For VP51, no flux calibrator was available, so we calibrated the flux on the phase calibrator, to which we assigned the value listed in Perley & Taylor (2003).